Phonovoltaic. III. Electron-phonon coupling and figure of merit of graphene:BN

Corey Melnick and Massoud Kaviany

Phys. Rev. B **94**, 245412 — Published 9 December 2016

DOI: 10.1103/PhysRevB.94.245412

Phonovoltaic III. Graphene:BN *e-p* coupling and figure of merit

Corey Melnick and Massoud Kaviany*

University of Michigan

Department of Mechanical Engineering

Ann Arbor, MI 48105-2125

Abstract

The phonovoltaic cell harvests optical phonons like a photovoltaic harvests photons. That is, a non-equilibrium (hot) population of optical phonons (at temperature $T_{p,\mathrm{O}}$) more energetic than the band gap produces electron-hole pairs in a *p-n* junction, which separates these pairs to produce power. A phonovoltaic material requires an optical phonon mode more energetic than its band gap and much more energetic than the thermal energy ($E_{p,\mathrm{O}} > \Delta E_{e,g} \gg k_\mathrm{B}T$), which relaxes by generating electrons and power (at rate $\dot{\gamma}_{e-p}$) rather than acoustic phonons and heat (at rate $\dot{\gamma}_{p-p}$). Graphene (h-C) is the most promising material candidate: when its band gap is tuned to its optical phonon energy without greatly reducing the electron-phonon (*e-p*) coupling, it reaches a substantial figure of merit [$Z_\mathrm{pV} = \Delta E_{e,g}\dot{\gamma}_{e-p}/E_{p,\mathrm{O}}(\dot{\gamma}_{e-p} + \dot{\gamma}_{p-p}) \approx 0.8$]. A simple tight-binding (TB) model presented here predicts that lifting the sublattice symmetry of graphene in order to open a band gap proscribes the *e-p* interaction at the band edge, such that $\dot{\gamma}_{e-p} \to 0$ as $\Delta E_{e,g} \to E_{p,\mathrm{O}}$. However, *ab initio* (DFT-LDA) simulations of layered h-C/BN and substitutional h-C:BN show that the *e-p* coupling remains substantial in these asymmetric crystals. Indeed, h-C:BN achieves a high figure of merit ($Z_\mathrm{pV} \approx 0.6$). At 300 K and for a Carnot limit of 0.5 ($T_{p,\mathrm{O}} = 600$ K), a h-C:BN phonovoltaic can reach an efficiency of $\eta_\mathrm{pV} \approx 0.2$, double the thermoelectric efficiency ($ZT \approx 1$) under similar conditions.

I. INTRODUCTION

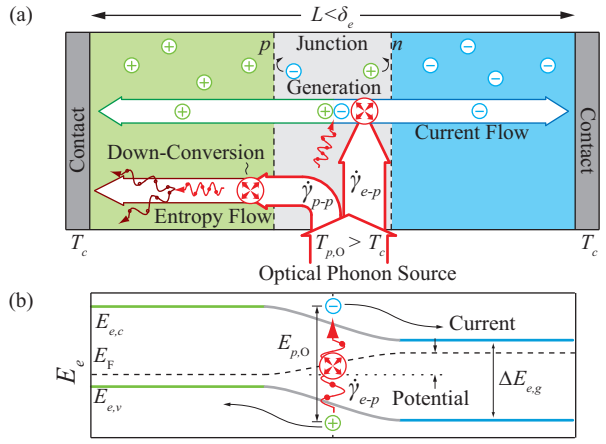

FIG. 1. (a) The phonovoltaic (pV) cell and (b) its energy diagram, which shows the quasi-Fermi level ($E_{\rm F}$), conduction and valence bands ($E_{e,c}$, $E_{e,v}$), and the generation of an electron-hole pair. In a pV, a source excites a population of optical phonon modes more energetic than the band gap in a p-n junction. This population relaxes by producing electrons (and power) or acoustic phonons (and heat).

The phonovoltaic (pV) cell harvests hot optical phonons like the photovoltaic harvests photons, as shown in Fig. 1 and described in Phonovoltaic I.[1] It is a nanoscale p-n junction (length L) with metal contacts attached to both the p and n sides (at temperature T_c). Within the junction, a source of optical phonons creates a non-equilibrium (hot) population of optical phonons (at temperature $T_{p,\rm O}$) more energetic than the band gap ($E_{p,\rm O} > \Delta E_{e,g}$) and hotter than the cold contacts ($T_{p,\rm O} > T_c$). This hot optical phonon population scatters with the valence electrons to generate electron-hole pairs. Then, the intrinsic field of the p-n junction separates them, forcing electrons (holes) towards the contact on the n (p) side. If the electrons reach and are collected by the contacts before they accumulate in the junction and inhibit further generation, then the device functions like a photovoltaic. That is, it functions like a diode with a supplied phono-current. Conversely, if cell is longer than the collection length ($\delta_e = \nu_e/\dot{\gamma}_{e-p}$, where ν_e is the electron velocity and $\dot{\gamma}_{e-p}$ is the rate of generation), then no significant non-equilibrium grows and the phonovoltaic acts like a thermoelectric, as discussed in Phonovoltaic I.[1] These two operational regimes are named the phonovoltaic and thermovoltaic regimes, respectively. Here, the search for a material

candidate which excels in the phonovoltaic regime continues. This search, which began in Phonovoltaic II[2], remains difficult, for a few reasons which are outlined below.

First, if the phonon mode is more energetic than the band gap, its extra energy ($E_{p,\mathrm{O}} - \Delta E_{e,g}$) is wasted; and if it is less energetic than the band gap, it can not generate electrons. Furthermore, the band gap and optical phonon must be substantially more energetic than the thermal energy; otherwise, the p-n junction to operates inefficiently, and the free carriers inhibit generation. Thus, the phonovoltaic requires a material with $E_{p,\mathrm{O}} \approx \Delta E_{e,g} \gg k_{\mathrm{B}}T$, where T is the cell temperature and k_{B} is the Boltzmann constant. As very few materials have a phonon mode more energetic than 100 meV, and even fewer of these have a small band gap, finding a promising material candidate is very challenging.

Further difficulties arise from the ability of a hot phonon population to relax through a variety of channels, which includes but is not limited to the generation of electron-hole pairs (at rate $\dot{\gamma}_{e-p}$). For example, optical phonons can down-convert into the acoustic modes (at rate $\dot{\gamma}_{p-p}$), heat the free-carriers (at rate $\dot{\gamma}_{e-p}^{\mathrm{intra}}$), and scatter with defects into unusable phonon modes (at rate $\dot{\gamma}_{p-d}$). These additional pathways generate heat rather than power. Thus, a pV material not only requires that $E_{p,\mathrm{O}} \approx \Delta E_{e,g} \gg k_{\mathrm{B}}T$, but it also requires that the rate of electron generation dominates the rate of heat generation ($\dot{\gamma}_{e-p} > \dot{\gamma}_{p\to q} = \dot{\gamma}_{p-p} + \dot{\gamma}_{e-p}^{\mathrm{intra}} + \dot{\gamma}_{p-d} + ...$). This narrows the field of material candidates further.

However, if a material candidate is found which meets these criteria, the benefits would be momentous: By intervening before a low-entropy optical phonon population spreads into the acoustic modes, gains a substantial amount of entropy, and becomes heat, the phonovoltaic can substantially outperform a thermoelectric device. Indeed, Phonovoltaic I[1] showed that the phonovoltaic cell can approach the Carnot limit (η_{C}), whereas the thermoelectric cells are limited, in practice, to around $0.2\eta_{\mathrm{C}}$. While the phonovoltaic cell may only reach between $0.5\eta_{\mathrm{C}}$ and $0.7\eta_{\mathrm{C}}$ at 300 K due to the limits in the phonon energy[1], this would be a massive step forward in steady-state heat harvest and recovery.

A. Phonovoltaic performance

Phonovoltaic I[1] showcased a simple, analytical, and physically intuitive pV efficiency (η_{pV}), based on the fraction of optical phonon energy preserved by the band gap ($\Delta E_{e,g}^{*} =$

$\Delta E_{e,g}/E_{p,\mathrm{O}}$) and the fraction of the hot optical phonons which relax by generating electrons rather than heat [$\dot{\gamma}^*_{e-p} = \dot{\gamma}_{e-p}/(\dot{\gamma}_{e-p} + \dot{\gamma}_{p\to q})$], the Carnot limit ($\eta_{\mathrm{C}}$), and the fill factor of the cell ($\mathrm{F_F}$). This efficiency is

$$\eta_{\mathrm{pV}} = \eta_{\mathrm{C}} \Delta E^*_{e,g} \dot{\gamma}^*_{e-p} \mathrm{F_F}, \tag{1}$$

where the Carnot limit is defined by the non-equilibrium between the hot optical phonon population ($T_{p,\mathrm{O}}$) and the cold contacts (T_c),

$$\eta_{\mathrm{C}} = 1 - \frac{T_c}{T_{p,\mathrm{O}}}. \tag{2}$$

A material figure of merit (Z_{pV}) is extracted from Eq. (1)

$$Z_{\mathrm{pV}} = \Delta E^*_{e,g} \dot{\gamma}^*_{e-p}, \tag{3}$$

such that the pV cell efficiency is limited by its material figure of merit and the Carnot limit. Noting that $\mathrm{F_F} \to 1$ as $\eta_{\mathrm{C}} \Delta E_{e,g}/k_{\mathrm{B}} T_c \to \infty$ and $\mathrm{F_F} \to 0.25$ as $\eta_{\mathrm{C}} \Delta E_{e,g}/k_{\mathrm{B}} T_c \to 0$, the pV efficiency only reaches $\eta_{\mathrm{C}} Z_{\mathrm{pV}}$ when there is substantial non-equilibrium ($\eta_{\mathrm{C}} \gg 0$) and the band gap is much larger than the thermal energy $\Delta E_{e,g} \gg k_{\mathrm{B}} T$.[1] Few materials can meet this criteria at 300 K, as discussed in the following section.

B. Phonovoltaic materials

The maximum optical phonon energy in a typical material is less than 50 meV.[3–5] Not only does this limit the band gap and thus the fill-factor of the phonovoltaic at higher temperatures, as discussed previously, but it also inhibits generation, as will be discussed in section III A. Only the semiconductors composed of first-row elements (e.g., Diamond and BN) exhibit an optical phonon more energetic than 150 meV. However, the strong bonds which produce these energetic phonons tend to localize electrons and open a band gap well over 1 eV. Even in softer semiconductors, the band gap is typically much larger than the optical phonon energy, as shown in Fig. 2. Thus, the optical phonons in a typical semiconductor either can not generate electron-hole pairs or can only generate them quickly under cryogenic conditions.

The sp^2 hybridized, group IV semiconductors (e.g., graphene) are a notable exception. In these materials, the symmetry between the two triangular sublattices creates the degenerate

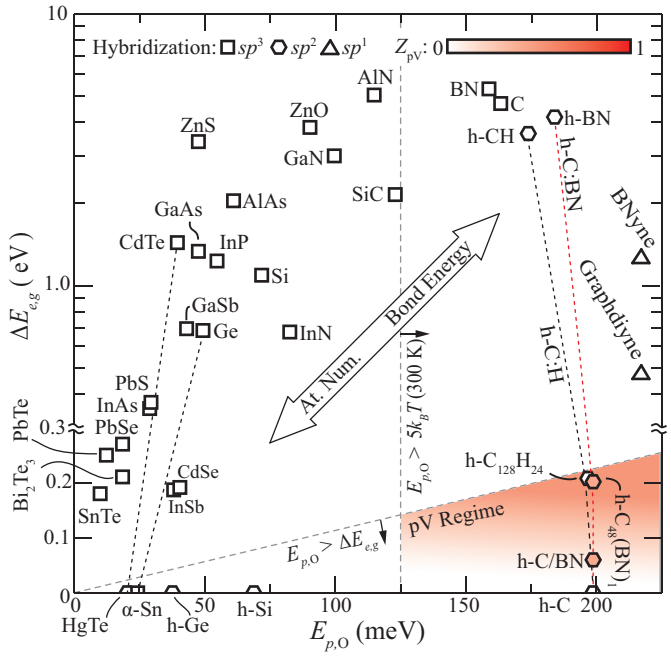

FIG. 2. The band gap and optical phonon energy of various semiconductors. An efficient pV requires $E_{p,\mathrm{O}} > \Delta E_{e,g} \gg k_{\mathrm{B}}T$, as in tuned graphene. In typical materials at 300 K, however, $\Delta E_{e,g} \gg E_{p,\mathrm{O}}$ or $E_{p,\mathrm{O}} \approx k_{\mathrm{B}}T$, as the strong bonds which enable energetic phonon modes also localize electrons and open a large band gap. The symmetry of group IV, sp^2 coordinated materials (e.g., graphene) enables them to overcome this trend. For traditional elemental and composite semiconductors, see [3–5]. For graphame (h-C:H), see [2,6]. For materials with the sp^1 acetylene bond, graphdiyne and BNyne, see [7,8]

Dirac points on the Fermi surface, and no band gap forms despite the strong sp^2 bonds.[9,10] Graphene, in particular, has extremely energetic optical phonon modes when compared to most materials, despite its semi-metallic nature. Crucially, there are many methods with which to open a band gap in graphene, and the e-p coupling dominates the p-p coupling.[11] If the properties of graphene were to remain constant as the band gap is tuned to the optical phonon energy, its pV figure of merit could exceed 0.8.[2] No other material candidate surveyed comes close to this promising figure of merit.

II. TUNING THE BAND GAP OF GRAPHENE

Opening a band gap in graphene has received substantial attention since its discovery, as many functional graphene devices require a band gap. Thus, researchers have proposed many methods to achieve this goal. For example, researchers have proposed the use of a large uniaxial strain[12–14], an electric or magnetic field[15,16], doping[17], an ordered substrate[18], or chemical functionalization[19] to open a band gap.

However, Phonovoltaic II[2] showed that opening a band gap in graphene can severely and negatively impact its interband *e-p* coupling. In particular, the use of hydrogenation to shift from sp^2 to sp^3 hybridization and open a band gap reduced the *e-p* coupling so severely that the figure of merit vanished. It is hypothesized that the change in hybridization was responsible, as the *e-p* coupling between the σ and σ^* bands is extremely weak in pure graphene. Thus, this study looks at the manipulation of the sublattice symmetry rather than the change in hybridization. This is done in general using a simple tight-binding model and in particular using the *ab initio* (DFT-LDA) simulation of graphene with boron and nitrogen atoms substituted into the lattice (h-C:BN) or placed below the graphene layer in a graphene/BN bilayer (h-C/BN).

A. Graphene:BN

When the symmetry between the two sublattices in graphene is disturbed, a band gap opens. In h-C:BN, carbon atoms in the crystal are replaced with a dilute concentration of boron and nitrogen atoms.[20–22] Electrons are attracted to the nitrogen atoms, or to the carbon atoms surrounding the boron atoms, due to the relative electronegativity of boron, carbon, and nitrogen. Ion-electron and electron-electron interactions propagate this perturbation throughout the lattice, such that the symmetry of the graphene lattice is removed and a band gap opens.[23] The more BN that is substituted into the lattice, the larger the band gap grows. Placing all of the boron atoms into one of the graphene sublattices and all of the nitrogen atoms into the other sublattice creates the largest band gap at a given BN concentration, as it maximizes the asymmetry created by the BN dopants.[23]

In theory, there is little reason to expect B and N atoms to order themselves at low concentration such that most B atoms are on one sublattice and most N atoms are on the

other sublattice. However, a low concentration of BN opens a relatively large band gap in experiments[24], larger than those predicted by density functional theory (DFT) simulations of h-C:BN with B and N on separate sublattices.[23] This is explained by the tendency of B and N atoms to clump into local $(BN)_n$ domains and also by the under-estimation of band gaps within DFT.[23]

Unfortunately, it is computationally impractical to calculate high-quality phonon and electron-phonon properties in large supercells. This limits the granularity and variety of h-C:BN crystals which can be reasonably simulated. Here, up to 6×6 graphene supercells are used with two distinct substitutional paradigms: ordered [h-$C_x(BN)_{y,o}$], wherein B and N are always on a different sublattice, and disordered [h-$C_x(BN)_{y,d}$], wherein B and N are

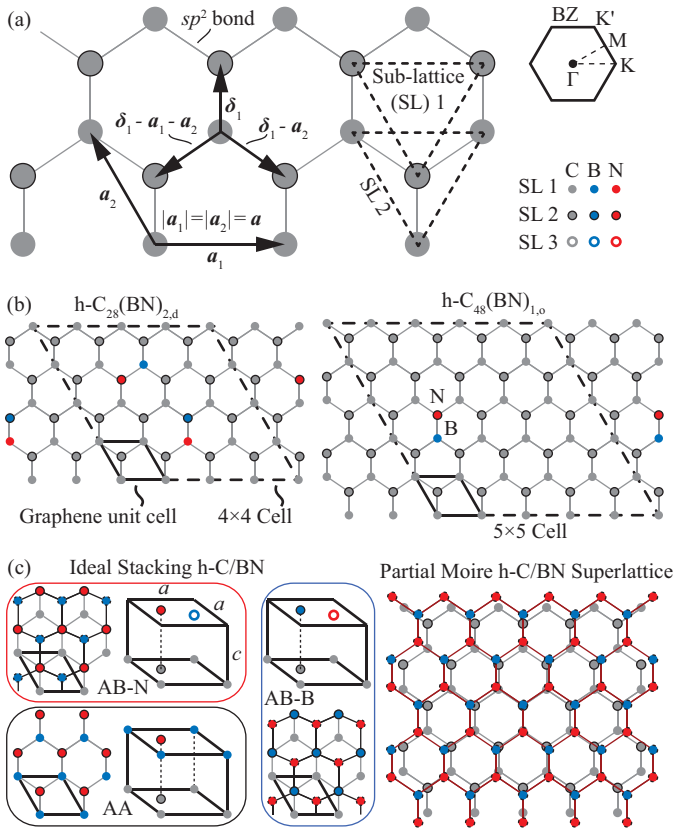

FIG. 3. (a) The graphene sheet, its geometry, and brillouin zone (BZ). In graphene, the sp^2 hybridized orbitals of carbon atoms form strong bonds with the three nearest neighbors in a hexagonal lattice (defined by two vectors a_1 and a_2 of length a) with two symmetric, triangular sublattices, separated by $\boldsymbol{\delta}_1$. (b) h-C/BN bilayers. Real bilayers form Moire superlattices rather than an ideally stacked structure due to the small difference in the h-C and h-BN lattice constants.

spread between the two sublattices. Two examples of these paradigms are shown in Fig. 3(b).

B. Graphene/BN

When a graphene sheet is placed on a h-BN substrate, such that each boron atom lies below a carbon atom in one sublattice and each nitrogen atom lies below a carbon atom in the other sublattice, as shown in Fig. 3(c), the cross-plane Van der Waals interactions remove the symmetry between these sublattices, and a band gap opens. However, h-BN has a slightly larger lattice constant than graphene, such that the bilayer forms a Moire superlattice, as shown in Fig. 3(c). This discrepancy spreads the boron – carbon and nitrogen – carbon interactions evenly between the two graphene sublattices, such that no net asymmetry arises, and no band gap opens.[25,26] While a bilayer of graphene on an h-BN substrate does exhibit a small band gap of 40 meV[25,26], the number of atoms required to simulate the h-C/BN superlattice prohibits *ab initio* phonon calculations.

Instead, the three ideal stacking configurations of h-C/BN are simulated here. These stacking configurations are as follows: AA stacking, where the B and N atoms are directly below the C atoms in graphene; AB-N stacking, where the N atoms are below the C atoms and the B atoms are under the vacancy in the graphene lattice; and AB-B stacking, where the B atoms are below the C atoms and the N atoms are under the vacancy, as shown in Fig. 3(c). Although these structures are non-physical (i.e., do not capture the lattice mismatch and its effects), simulating them helps to investigate the relationship between the asymmetry, band gap, and *e-p* coupling in tuned graphene materials. Moreover, the small unit cell enables the *p-p* coupling calculations which remain out-of-reach for the large h-C:BN supercells.

III. CENTRAL MECHANISMS

Central to the successful operation of the pV and the material figure of merit is the interband electron-phonon coupling which drives electron generation, and the competing interactions which produce heat. These interactions include the intraband electron-phonon coupling, wherein a free charge gains kinetic energy after absorbing a phonon; the phonon-

phonon coupling, wherein an optical phonon down-converts into two acoustic phonons; and the phonon-defect coupling, wherein an optical phonon scatters with a defect to produce high momentum phonons incapable of generating electrons. In this section, these four mechanisms are discussed.

A. The Electron-phonon coupling

As a phonon displaces the ions in a crystal, it changes the electric potential-field created by those ions. Electrons around the displaced ions can scatter against the perturbed potential and absorb the phonon.[27] The electron-phonon coupling describes this interaction (as well as phonon emission). The *e-p* interaction element follows from perturbation theory is[28]

$$M_{ep,\alpha,i,j}(\boldsymbol{k}_e,\boldsymbol{k}_p) = (\frac{\hbar}{2m\omega_{\boldsymbol{k}_p,\alpha}})^{1/2}\langle \boldsymbol{k}_e+\boldsymbol{k}_p, j|\frac{\partial\varphi_e}{\partial \boldsymbol{d}_{\boldsymbol{k}_p,\alpha}}|\boldsymbol{k}_e, i\rangle, \tag{4}$$

where i and j are the initial and final band indices, φ_e is the electron potential energy, m is the atomic mass, and $\omega_{\boldsymbol{k}_p,\alpha}$ and $\boldsymbol{d}_{\boldsymbol{k}_p,\alpha}$ are the frequency and atomic displacement pattern of a phonon with momentum $\boldsymbol{k}_p$ and polarization α. The first group of terms describes the displacement of the phonon mode and the second quantifies the change in potential where initial and final electron states overlap. Thus, a strong *e-p* coupling requires, at minimum, that the valence and conduction states overlap substantially.

The Fermi golden rule (FGR)[29] turns this coupling element into an *e-p* scattering rate ($\dot{\gamma}_{e-p}$), i.e.,

$$\dot{\gamma}^{\pm}_{e-p}(\boldsymbol{k}_p,\alpha) = \frac{2\pi}{\hbar}\sum_{\boldsymbol{k}_e,ij}|M_{ep,\alpha,i,j}(\boldsymbol{k}_e,\pm\boldsymbol{k}_p)|^2\delta[E_{e,i}(\boldsymbol{k}_e)-E_{e,j}(\boldsymbol{k}_e\pm\boldsymbol{k}_p)\pm\hbar\omega_{\boldsymbol{k}_p,\alpha}] \tag{5}$$

$$\times[f_{e,i}(\boldsymbol{k}_e)-f_{e,j}(\boldsymbol{k}_e\pm\boldsymbol{k}_p)], \tag{6}$$

where the $+$ $(-)$ indicates absorption (emission), and $E_{e,i}(\boldsymbol{k}_e)$ and $f_{e,i}(\boldsymbol{k}_e)$ are the energy and occupation of an electron in band i and with momentum $\boldsymbol{k}_e$.

The occupation terms have important consequences. Primarily, if the band gap is much larger than $k_{\mathrm{B}}T$ and the Fermi level is far from the valence and conduction band edges, the intraband interactions are substantially reduced by either the lack of conduction electrons [$f_{e,c}(\boldsymbol{k}_e)\simeq 0$] or by the lack of empty states in the valence band [$f_{e,v}(\boldsymbol{k}_e)\simeq f_{e,v}(\boldsymbol{k}_e\pm\boldsymbol{k}_p)\simeq 1$]. Conversely, if the band gap is much smaller than $k_{\mathrm{B}}T$ or if doping moves the Fermi level into the conduction or valence bands, the interband interaction is inhibited by the lack of

empty states in the conduction band or the lack of electrons in the valence band. Moreover, as the band gap approaches the optical phonon energy, the number of available energy conserving states approaches zero. Thus, strong interband coupling requires that the band gap is smaller than the phonon energy and that the phonon energy is substantially larger than $k_{\mathrm{B}}T$, i.e., $E_{p,\mathrm{O}} > \Delta E_{e,g} \gg k_{\mathrm{B}}T$.[2]

1. *Intraband scattering*

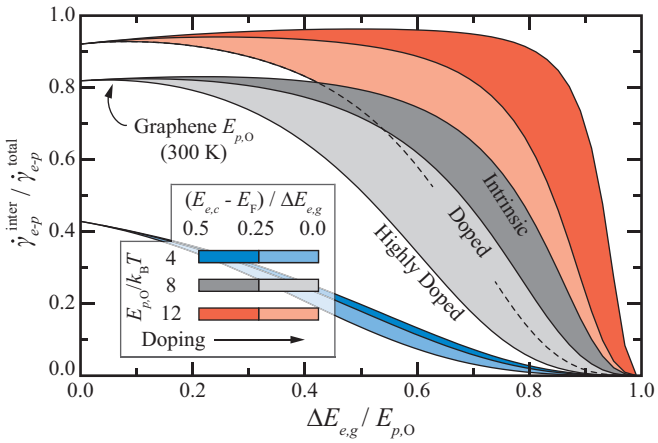

FIG. 4. The ratio of the interband generation rate to the total rate of optical phonon absorption by electrons in graphene. When the optical phonon energy is much larger than $k_{\mathrm{B}}T$ in an intrinsic semiconductor, the rate of interband generation events dominates the rate of intraband heating events until $\Delta E_{e,g} \to E_{p,\mathrm{O}}$. As the optical phonon energy approaches $k_{\mathrm{B}}T$ or as the Fermi level approaches the conduction band edge ($E_{\mathrm{F}} \to E_{e,c}$), the interband interactions dominate over a much smaller range of band gap energies. When $E_{p,\mathrm{O}}/k_{\mathrm{B}}T < 5$, the intraband interactions always dominate.

As previously noted, intraband phonon absorption events heat the electron population and do not contribute to power production. Therefore, they can reduce the material figure of merit. However, these events can be neglected, and the summation in Eq. (6) is safely restricted to the interband indices, in three instances.

First, intraband scattering events heat the optical phonon population, rather than cooling it. For example, when electrons (holes) are excited into energetic conduction (valence) states by an electric field, they emit optical phonons as they relax, which heats the optical phonon

population. In this case, the intraband interactions do not act as a undesirable relaxation pathway. Rather, they act as the source of optical phonons required for pV operation, and the intraband coupling can be substantial without affecting Z_{pV}.

Second, the collection of hot optical phonon modes are limited to momenta which enable energy conservation for inter- but not intraband transitions, such that the intraband interaction rate is zero. For example, only interband *e-p* interactions occur in graphene when $\boldsymbol{k}_p < E_{p,\mathrm{O}}/(|\nu_e|\hbar)$, where ν_e is the electron Fermi velocity. Conversely, if the interband transition is forbidden by momentum and energy conservation, but the intraband interaction is allowed, then intraband interactions dominate. For example, only intraband interations occur in graphene when $\boldsymbol{k}_p > E_{p,\mathrm{O}}/(|\nu_e|\hbar)$.

Third, there are substantially more electrons near the valence band edge than there are holes or conduction electrons, i.e., $E_{p,\mathrm{O}} > \Delta E_{e,g} \gg k_{\mathrm{B}}T$ and under moderate doping. To quantify this condition, consider a material where the inter- and intraband coupling elements have similar magnitude throughout the brillouin zone (BZ), i.e., $|M_{ep,\alpha,c,v}| \approx |M_{ep,\alpha,c,c}| \approx |M_{ep,\alpha,v,v}|$, where c and v represent the conduction and valence band indices. Next, assume that the phonon of interest is an optical mode ($\alpha = \mathrm{O}$) near the Γ-point with negligible group velocity ($\hbar\omega_{\hbar\boldsymbol{k}_p,\mathrm{O}} \simeq E_{p,\mathrm{O}}$ when $\boldsymbol{k}_p \approx 0$). Further assume that the electron distribution is given by Fermi-Dirac statistics (f_e°) and that the electron density of states (D_e) near valence and conduction band edges are identical. Finally, note that the total scattering rate involves a summation over $\boldsymbol{k}_p$ as well as $\boldsymbol{k}_e$. That is, Eq. (6) gives the rate at which a particular phonon mode ($\boldsymbol{k}_p$, α) scatters with all of the electrons, while the total rate considers the scattering of a particular polarization (α) with all of the electrons.

These summations and the δ-function are transformed into an integral over the electron energy using two electron density of state (D_e) functions representing the initial and final density of states. Through this procedure[2], the ratio of inter- to intraband phonon absorption

events is quantified as

$$\frac{\dot{\gamma}_{e-p}^{\text{inter}}}{\dot{\gamma}_{e-p}^{\text{intra}}} = \Big\{ \int_0^{E_{p,\text{O}}-\Delta E_{e,g}} \mathrm{d}E_e D_e(E_{p,\text{O}} - \Delta E_{e,g} - E_e) D_e(E_e) \times [f_e^\circ(-E_e - \Delta E_{\text{F,v}}) - f_e(E_{p,\text{O}} - \Delta E_{e,g} - E_e + \Delta E_{\text{F,c}})] \Big\} / \Big\{ \int_0^\infty \mathrm{d}E_e D_e(E_e) D_e(E_e + E_{p,\text{O}}) \times [f_e^\circ(E_e + \Delta E_{\text{F,c}}) - f_e^\circ(E_e + \Delta E_{\text{F,c}} + E_{p,\text{O}}) + f_e^\circ(-E_e - E_{p,\text{O}} - \Delta E_{\text{F,v}}) - f_e^\circ(-E_e - \Delta E_{\text{F,v}})] \Big\}, \tag{7}$$

where $\Delta E_{\text{F,v}} = E_{\text{F}} - E_{e,v}$ and $\Delta E_{\text{F,c}} = E_{e,c} - E_{\text{F}}$ are the energy differences between the valence ($E_{e,v}$) and conduction ($E_{e,c}$) band edges and the Fermi level (E_{F}). Note that the intraband scattering rate includes both hole and electron contributions.

Figure 4 shows the importance of intraband scattering for the dispersionless bands of graphene ($D_e \propto |E_e|$) as predicted by Eq. (7). Note that adding dispersion (e.g., $D_e \propto |E_e|^{1/2}$) to the bands increases the density of the low-energy states relative to the high-energy states. Thus, it decreases the relative importance of the intraband scattering events, and Fig. 4 provides conservative results.

Despite this, it shows that the interband interactions dominate when $E_{p,\text{O}} \gg k_{\text{B}}T$, unless the Fermi level moves extremely close to the band edges or the band gap approaches the phonon energy. For $E_{p,\text{O}}/k_{\text{B}}T < 10$, however, the intraband scattering events begin to compete with generation events. For $E_{p,\text{O}}/k_{\text{B}}T < 5$ the intraband scattering events dominate the generation events, regardless of the band gap or amount of doping.

In this study, it is assumed that at least one of these three cases hold. Typically, an excited electron population produces the hot optical phonon population as it relaxes. Thus, the first conditions is met. Moreover, the second conditions is always met when the figure of merit is evaluated for a Γ-point phonon, as it is here. Finally, the third condition can be met under certain conditions, even at 300 K, as outlined by Fig. 4. Thus, this assumption is typically reasonable.

B. Phonon-phonon coupling

The *p*-*p* coupling arises from the anharmonicity of the crystal, and it is typically dominated by the three-phonon interactions[30]: up-conversion, where two low-energy phonons

combine to create a single high-energy phonon, and down-conversion, where a high-energy phonon scatters with and creates two low-energy phonons. The three-phonon coupling arises from the third-order derivatives of the crystal energy (Ψ).[31] Thus, the matrix element for the interaction between three phonons is

$$M^{\boldsymbol{k}_p\boldsymbol{k}'_p\boldsymbol{k}''_p}_{\alpha\alpha'\alpha''} = \sum_{ijk}\sum_{xyz}\left(\frac{\hbar}{2m_i m_j m_k \omega_{\boldsymbol{k}_p,\alpha}\omega_{\boldsymbol{k}_p{}',\alpha'}\omega_{\boldsymbol{k}_p{}'',\alpha''}}\right)^{3/2}\Psi^{xyz}_{ijk}\epsilon^{xi}_{\boldsymbol{k}_p,\alpha}\epsilon^{yj}_{\boldsymbol{k}'_p,\alpha''}\epsilon^{zk}_{\boldsymbol{k}'_p,\alpha''}\delta_{\boldsymbol{k}_p,\boldsymbol{k}'_p\pm\boldsymbol{k}''_p}, \quad (8)$$

where $\epsilon^{xi}_{\boldsymbol{k}_p,\alpha}$ is the polarization of the phonon mode in the x direction for atom i, Ψ^{xyz}_{ijk} is the partial derivative of the crystal energy for the displacement of atoms i, j, and k in directions x, y, and z, and the δ-function conserves momentum during up- ($-$) and down-conversion ($+$). Note that the dynamical matrix describing the phonon modes arises from the second-order derivatives of the crystal energy.

The rate of down-conversion [$\gamma_{p-p}(\boldsymbol{k}_p,\alpha)$] resulting from this interaction follows from the FGR. For a zone-center phonon mode, the FGR gives[32]

$$\dot{\gamma}_{p-p}(\Gamma,\alpha) = \frac{2\pi}{N_{\boldsymbol{k}_p{}'}}\sum_{\alpha'\alpha''\boldsymbol{k}'_p}|M^{\Gamma\boldsymbol{k}'_p-\boldsymbol{k}'_p}_{\alpha\alpha'\alpha''}|^2\delta(\omega_{\Gamma,\alpha}-\omega_{\boldsymbol{k}'_p,\alpha'}-\omega_{\boldsymbol{k}'_p,\alpha''})(f'_p+f''_p+1), \quad (9)$$

where f_p is the phonon occupation. The occupation terms indicate that down-conversion is enhanced the hotter the cell becomes and the less energetic the final states are. Thus, down-conversion is reduced when the optical phonon mode is much more energetic than the thermal energy and, again, $E_{p,\mathrm{O}} \gg k_\mathrm{B}T$ is desired.

C. Phonon-defect coupling

Defects in a crystal, e.g., the B and N atoms in h-C:BN, act as scattering centers for the phonons of the ideal crystal. In general, a defect can have a different mass than the atoms in the ideal crystal, or it can change the interatomic force constants. These variations lead to local changes in the atomic displacement and the frequency of this displacement, creating a scattering center. Moreover, the variations are typically random, rather than ordered, such that the momentum conservation enforced in the *e-p* and *p-p* couplings do not apply here. That is, only energy is conserved in the phonon-defect coupling.[33]

The matrix element which arises from a change in mass, e.g., when isotopes are distributed

throughout the crystal, is[34]

$$M_{p-i,\alpha\alpha'}(\boldsymbol{k}_p, \boldsymbol{k}_p{}') = [x(1-x)(\frac{\delta m}{\overline{m}})]^{1/2}\omega_{\boldsymbol{k}_p,\alpha}\sum_i |\boldsymbol{\epsilon}^{i*}_{\boldsymbol{k}_p,\alpha}\cdot\boldsymbol{\epsilon}^{i}_{\boldsymbol{k}_p',\alpha'}|, \tag{10}$$

where x is the disorder parameter, i.e., the probability an atom at site i has mass $m+\delta m$, and $\overline{m}$ is the average mass. From the FGR, the rate of isotopic scattering becomes

$$\dot{\gamma}_{p-i,\alpha}(\boldsymbol{k}_p) = \frac{\pi}{2N_{\boldsymbol{k}_p{}'}}\sum_{\boldsymbol{k}_p{}',\alpha'}|M_{id,\alpha\alpha'}(\boldsymbol{k}_p,\boldsymbol{k}_p{}')|^2\delta(\omega_{\boldsymbol{k}_p,\alpha}-\omega_{\boldsymbol{k}_p{}',\alpha'}). \tag{11}$$

However, this interaction element does not account for changes to the inter-atomic force constants, and it is difficult to derive a satisfactory and reasonable matrix element which includes the complete effects a cluster of BN atoms has when substituted into graphene. Thus, instead of the perturbation approach used for the previous scattering mechanisms, a Green's function approach is taken.[34,35]

In this approach, the phonon spectral function $[A_{\boldsymbol{k}_p\alpha}(\omega)]$ is evaluated, and its full-width at half-maximum is the scattering rate. The spectral function is given by

$$A_{\boldsymbol{k}_p,\alpha}(\omega) = -\frac{1}{\pi}\mathrm{Im}[G_{\boldsymbol{k}_p,\alpha}(\omega)] \tag{12}$$

$$G_{\boldsymbol{k}_p,\alpha}(\omega) = \langle\boldsymbol{\epsilon}_{\boldsymbol{k}_p,\alpha}|\frac{2\omega}{(\omega+i\zeta)^2-\boldsymbol{D}}|\boldsymbol{\epsilon}_{\boldsymbol{k}_p,\alpha}\rangle, \tag{13}$$

where $\boldsymbol{D}$ is the *ab initio* dynamical matrix of the h-C:BN crystal, $\boldsymbol{\epsilon}_{\boldsymbol{k}_p,\alpha}$ are the normalized eigenvectors of the dynamical matrix of the ideal graphene crystal, and ζ is a small, positive number.

IV. TIGHT BINDING MODEL

Before proceeding onto the *ab initio* analysis, it is useful to determine the expected results. Here, a simple tight binding model is presented in order to determine how the sublattice symmetry effects the band structure and electron-phonon coupling.

The tight binding (TB) model assumes each electron in the crystal is tightly bound to the ions in that crystal and that the remaining electron interactions are comparatively small. Thus, the Hamiltonian (H_{TB}) is

$$H_{\mathrm{TB}} = \sum_m H_{at,m} + \Delta H, \tag{14}$$

where $H_{at,m}$ is the isolated atomic Hamiltonian of atom m and ΔH represents the remaining interactions of the crystal, with $H_{at,m} \gg \Delta H$. Thus, the electron wavefunctions (ψ) are built using a linear combination of Bloch functions (Φ_{mn}) based on the atomic orbitals (ϕ_{mn}) which satisfy $H_{at,m}\phi_{mn} = \epsilon_{mn}\phi_{mn}$, where ϵ_{mn} is the energy of the n^{th} orbital for atom m. That is,

$$\psi_{\boldsymbol{k}_e}(\boldsymbol{r}) = \sum_{mn} \beta_{mn}\Phi_{mn} \tag{15}$$

$$\Phi_{mn} = \frac{1}{N^{1/2}} \sum_{l} \phi_{mn}(\boldsymbol{r} - \boldsymbol{R}_{lm}) e^{i\boldsymbol{k}_e \cdot \boldsymbol{R}_{lm}}, \tag{16}$$

where β_{mn} is the weight of each Bloch function, which combines the atomic orbitals of each atom at location $\boldsymbol{R}_{lm}$ in the $l = 1, 2, ..., N$ unit cells.

The tight-binding approach has been been widely and successfully used to model the band structure of graphene.[36–38] A simple model which accurately reproduces the band structure near the Fermi surface assumes that the bonding sp^2 orbitals (s, p_x, and p_y) form the deep valence and energetic conduction bands (σ and σ^* bands), while the remaining p_z orbitals form the near-Fermi band structure (π and π^* bands). Moreover, it assumes that these two sets of orbitals do not interact. Thus, the basis is safely constrained to a single p_z orbital per atom, i.e.,

$$\psi_{n\boldsymbol{k}_e}(\boldsymbol{r}) = |\boldsymbol{k}_e\rangle = \sum_{m} \beta_m \Phi_m = \frac{1}{N^{1/2}} \sum_{l} p_{z,m}(\boldsymbol{r} - \boldsymbol{R}_{lm}) e^{i\boldsymbol{k}_e \cdot \boldsymbol{R}_{lm}}. \tag{17}$$

Further, it assumes these atomic orbitals are orthogonal, such that $\langle p_{z,m}|p_{z,m'}\rangle = \delta_{m,m'}$ and

$$\langle \boldsymbol{k}_e{}'|H_{\text{TB}}|\boldsymbol{k}_e\rangle = \epsilon_{\boldsymbol{k}_e}\delta_{\boldsymbol{k}_e{}',\boldsymbol{k}_e}. \tag{18}$$

Finally, it assumes ΔH only contains the interactions between the orbital centered on one atom and the ionic potential of its nearest neighbor ions ($\varphi_{\text{ion,m}'}$), i.e.,

$$\langle p_{z,m'}|\Delta H|p_{z,m}\rangle = \int \mathrm{d}\boldsymbol{r}\, p_{z,m'}(r - \boldsymbol{R}_{m'})\varphi_{\text{ion},m}(r) p_{z,m}(r - \boldsymbol{R}_m) = -\varphi_h, \tag{19}$$

when m and m' are nearest neighbor atoms. Otherwise, the integral is zero. φ_h, the hopping integral, describes the tendency for an electron to hop from one atomic orbital to its nearest neighbor.

It follows from Eqs. (17 and 18) that the 2×2 matrix formed by $H_{ij} = \langle \Phi_i|H_{\text{TB}}|\Phi_j\rangle$ has eigenvalues $\epsilon^{\pm}_{\boldsymbol{k}_e}$ and eigenvectors $\boldsymbol{\beta}_{\pm} = (\beta_1, \beta_2)$, which represent the valence ($-$) and conduction bands ($+$). That is,

$$\boldsymbol{H} - \epsilon_{\boldsymbol{k}_e}\boldsymbol{I} = 0, \tag{20}$$

where $\boldsymbol{I}$ is the identity matrix. The diagonal elements of $\boldsymbol{H}$ capture the self energy (ϵ_i) of the atomic orbitals, while the off-diagonals capture the hopping strength (φ_h) modified by a phase-factor (γ), i.e.,

$$\boldsymbol{H} = \begin{bmatrix} \epsilon_1 & \varphi_h\gamma(\boldsymbol{k}_e) \\ \varphi_h\gamma^*(\boldsymbol{k}_e) & \epsilon_2 \end{bmatrix}. \tag{21}$$

The phase-factors capture the effects of the geometry on the Bloch waves, i.e.,

$$\gamma = \sum \exp(i\boldsymbol{k}_e \cdot \boldsymbol{\delta}_i), \tag{22}$$

where $\boldsymbol{\delta}_i$ is a vector connecting nearest-neighbors, as shown in Fig. 3(a). That is, $\boldsymbol{\delta}_1 = a(0, 3^{1/2}/3, 0)$, $\boldsymbol{\delta}_2 = \boldsymbol{\delta}_1 - \boldsymbol{a}_1$, and $\boldsymbol{\delta}_3 = \boldsymbol{\delta}_1 - \boldsymbol{a}_1 - \boldsymbol{a}_2$ connect an atom on one sublattice with its nearest neighbors, where a is the lattice constant and $\boldsymbol{a}_1 = a(1, 0, 0)$ and $\boldsymbol{a}_2 = a(-0.5, 3^{1/2}/2, 0)$ are the vectors defining a hexagonal unit cell.

$\boldsymbol{H}$ has eigenvalues (describing the electron bands)

$$\epsilon^{\pm}_{\boldsymbol{k}_e} = \frac{1}{2}\{\epsilon_1 + \epsilon_2 \pm \varphi_h[12\varphi_h^2 + (\epsilon_1 - \epsilon_2)^2 + 8\varphi_h^2(2\cos\frac{\kappa_{e,x}}{2} + \cos\frac{3^{1/2}\kappa_{e,y}}{2} + \cos 3^{1/2}\kappa_{e,y})]^{1/2}\}, \tag{23}$$

and eigenvectors (describing the electron wavefunctions)

$$\begin{aligned} \beta_1^{\pm} &= 1 \\ \beta_2^{\pm} &= \frac{2\epsilon^{\pm}_{\boldsymbol{k}_e} - \epsilon_1}{2t(1 + 2\exp\frac{i\kappa_{e,x}}{2}\cos\frac{3^{1/2}\kappa_{e,y}}{2})}, \end{aligned} \tag{24}$$

where the + (−) denotes a value associated with the conduction (valence) band.

A. Results

In graphene, and in the other Group IV hexagonal materials, both atoms in the unit cell are identical, such that $\epsilon_1 = \epsilon_2$. Under this symmetry, the conduction and valence bands are degenerate (no band gap) and the electron has zero effective mass near these Dirac points (at K and K′), as shown in Fig. 5. This leads to many of the remarkable material properties in graphene. In addition, the TB model predicts that both of the Bloch functions contribute equally to the conduction and valence band wavefunctions throughout the BZ ($|\beta_1^{\pm}| = |\beta_2^{\pm}|$). That is, the wavefunction is spread equally between all p_z orbitals, regardless of $\boldsymbol{k}_e$ and $\epsilon^{\pm}_{\boldsymbol{k}_e}$.

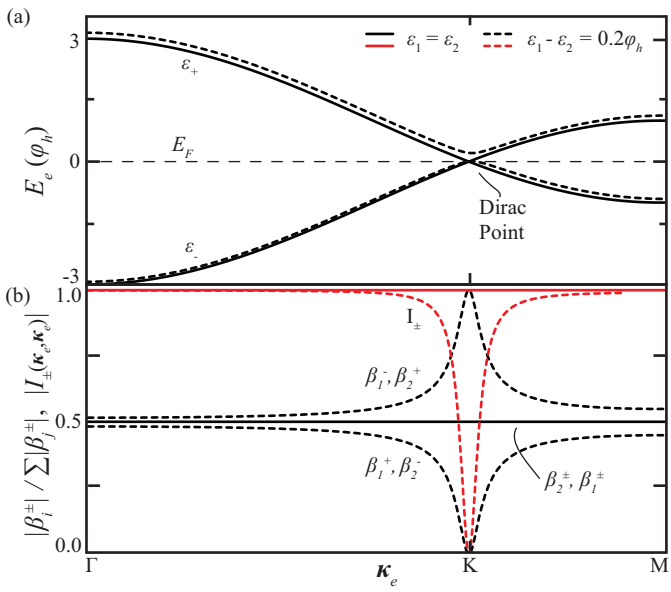

FIG. 5. (a) The band structure ($\epsilon_\pm$) and (b) fraction of the electron wavefunction composed by atomic orbitals centered on atoms in one of the two sublattices ($|\beta_i^\pm| / \sum |\beta_i^\pm|$) and resulting overlap ($I^\pm_{\boldsymbol{k}_e, \boldsymbol{k}_e'}$) of the valence (-) and conduction(+) bands with (—) and without (--) sublattice symmetry. In a symmetric crystal like graphene, no gap exists and the valence- and conduction-band wavefunctions overlap. In a non-symmetric crystal like h-BN, a band gap opens, the valence and conduction bands collapse into atomic orbitals centered on different sublattices, and the overlap between them vanishes at the band edge, proscribing the *e-p* interaction.

The symmetry between the two sublattices creates these phenomena. As there is no energy cost associated with an electron moving from one set of orbitals to the other, the electrons are not localized to one set of orbitals. Thus, the wavefunction is a mix of both atomic orbitals. Moreover, the electrons are free to and always do move throughout the lattice.

However, when the symmetry between the two atomic sites is broken, such that $\epsilon_1 \neq \epsilon_2$, the degeneracy between the conduction and valence bands is lifted, a band gap opens ($\Delta E_{e,g} = \varphi_h |\epsilon_1 - \epsilon_2|$), and the electrons gain an effective mass at K and K′ (the former Dirac points and the new band edge). Furthermore, the wavefunction at the valence (conduction) band edge collapses into the Bloch wavefunction composed of the less (more) energetic atomic orbitals, as shown in Fig. 5(b).

This wavefunction collapse is most intuitively understood through an excitation picture.

Consider a valence electron at band edge in an asymmetric crystal, which is given just enough energy to surmount the band gap, scatter into the conduction band, and leave a hole behind. As this electron has no energy remaining to move about the crystal (no kinetic energy), it must be localized to one of the two sets of atomic orbitals. Likewise, the hole it leaves behind has no kinetic energy and must also be localized. It is intuitive that the hole (electron) is localized to the set of orbitals with less (more) self-energy. Then, as these excitations gain kinetic energy, i.e., move through the crystal, they must also become delocalized. Therefore, their wavefunctions must mix with the previously unoccupied orbitals.

This has important consequences on the interband *e-p* coupling in asymmetric crystals. Consider the interband interaction element from Eq. (4) for a Γ-point

$$M_{ep,\alpha,+,-}(\boldsymbol{k}_e,\Gamma) \propto \langle \boldsymbol{k}_e,+|\frac{\partial \varphi_e}{\partial \boldsymbol{d}_{\Gamma,\alpha}}|\boldsymbol{k}_e,-\rangle. \tag{25}$$

Assuming that $\partial\varphi_e/\partial \boldsymbol{d}_{\boldsymbol{k}_p,\Gamma}$ is relatively constant throughout the cell, the interaction element is proportional to the overlap between the initial and final electron wavefunction ($I^{\pm}_{\boldsymbol{k}_e,\boldsymbol{k}_{e'}}$)

$$M_{ep,\alpha,+,-}(\boldsymbol{k}_e,\Gamma) \propto \langle \boldsymbol{k}_e,+|\boldsymbol{k}_e,-\rangle = I^{\pm}_{\boldsymbol{k}_e,\boldsymbol{k}_{e'}}. \tag{26}$$

Using Eqs. (17 and 18), the TB overlap integral is

$$I^{\pm}_{\boldsymbol{k}_e,\boldsymbol{k}_{e'}} = \sum_i |\overline{\beta}_i^{+}||\overline{\beta}_i^{-}|, \tag{27}$$

where $\overline{\beta}_i^{\pm}$ is the normalized $\beta_i^{\pm}$. Thus, the collapse of the conduction and valence wavefunctions into orthogonal atomic orbitals prohibits the *e-p* interaction at, and weakens it near, the band edge (K and K′). Throughout most of the BZ, however, the TB overlap integral remains near unity, as shown in Fig. 5.

V. *AB INITIO* RESULTS

The tight-binding model makes several key assumptions, e.g., that changes to the overlap integral dominate changes to the *e-p* interaction and that the two sets of atomic orbitals are orthogonal. Therefore, it remains crucial to test its predictions. Here, the *ab initio* simulation of graphene, h-BN, h-C:BN, and graphene/BN is used for this purpose and in an effort to find and characterize a suitable pV material. Therefore, the TB model predicts that $\dot{\gamma}_{e-p} \to 0$ as $\Delta E_{e,g} \to E_{p,\mathrm{O}}$, but remains unaffected as $\Delta E_{e,g} \to 0$.

A. Methods

The density functional theory (DFT) and density functional perturbation theory (DFPT) calculations are done using Quantum Espresso[39], the local density approximation (LDA) for the exchange-correlation functional, norm conserving pseudopotentials generated by the Martins-Toullier method[40], and a plane-wave basis with a 55 Ry cut-off frequency. A 30×30 $\boldsymbol{k}_e$-mesh is used for graphene, h-BN, and h-C/BN crystals, while a 9×9 $\boldsymbol{k}_e$-mesh is used for the 4×4 h-C:BN supercells (32 atoms) and a 6×6 $\boldsymbol{k}_e$-mesh is used for the larger h-C:BN supercells. Phonon properties are calculated on a 15×15 $\boldsymbol{k}_p$ mesh for graphene and h-C/BN and at the Γ-point of the h-C:BN crystals.

A lattice constant of 2.43 Å is used for all structures: While h-BN has a slightly larger lattice constant than graphene, a less than 6% concentration of BN should have a negligible impact on overall lattice constant. The graphite inter-layer spacing of 3.22 Å is used for the h-C/BN simulations. All structures are surrounded by at least 12 Å of vacuum. Before further calculation, the atoms are relaxed within the crystal until all force components converge to within 10^{-6} Ry/Å and the energy converges to within 10^{-8} Ry.

B. Electron and Phonon properties

Following these methods, the electron band gap and band structure are calculated for h-C, h-BN, a variety of h-C:BN crystals, and the three ideal h-C/BN stacking configurations. Then, the phonon properties are calculated h-C, h-BN, and for those h-C:BN and h-C/BN crystals which have a band gap in the range of interest [$\Delta E_{e,g} \in (0, E_{p,\mathrm{O}})$].

1. Band gap

A variety of the simulated h-C:BN and all h-C/BN crystals have band gap that lies in range of interest, i.e., $\Delta E_{e,g} < E_{p,\mathrm{O}}$, as shown in Fig. 6. In particular, the ordered h-$C_{48}(BN)_{1,o}$ has a band gap extremely close to the optical phonon energy, while the disordered h-$C_{28}(BN)_{2,d}$ has an extremely small band gap. The h-$C_{70}(BN)_{1,o}$, h-$C_{68}(BN)_{2,o}$, and the h-C/BN structures have band gaps spaced across $0.20E_{p,\mathrm{O}} < \Delta E_{e,g} < 0.8E_{p,\mathrm{O}}$. Thus, this collection of crystals enables a reasonable investigation of the *e-p* coupling in tuned graphene.

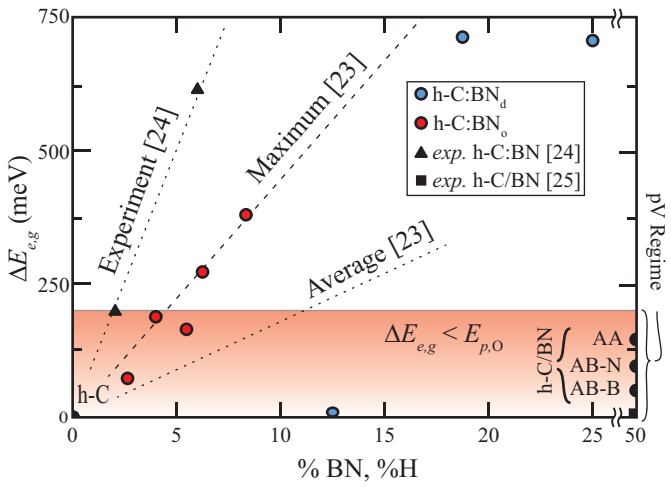

FIG. 6. The band gap of h-C:BN and h-C/BN for variations in the BN concentration. The band gap tends to increase as the concentration increases, particularly when the B and N atoms are substituted into different sublattices (ordered h-C:BN$_o$), as previously predicted.[23] Conversely, the band gap widens slowly with the disordered substitution of BN onto random sublattices (h-C:BN$_d$). The experimental results[24] show that the gap widens even more quickly than in h-C:BN$_o$. Regardless, a few of the simulated crystals meet the primary pV condition: $E_{p,\mathrm{O}} > \Delta E_{e,g}$.

As discussed in Sec. II A, the ordered placement of B and N atoms onto separate sublattices (h-C:BN$_o$) maximizes the band gap, while their disordered placement (h-C:BN$_d$) minimizes the band gap. Indeed, the band gap of h-C:BN$_o$ approaches the maximum value predicted by Nascimento *et al.*, as shown in Fig. 6.[23] However, the band gap of the h-C:BN$_o$ crystals remains well below the experimental trend.[24] Indeed, experimental results suggest that only a 2% BN concentration is required to tune the band gap of h-C:BN to its optical phonon mode (200 meV), while h-C:BN$_o$ requires a BN concentration of 5% to reach 200 meV in these simulations. This is likely due to the underestimation of the band gap within DFT-LDA simulations.

The h-C/BN structures, in contrast, diverge from both previous *ab initio* and experimental results.[25,26] This is expected: as discussed in Sec. II B, the real crystal forms a Moire superlattice, not the ideally stacked configurations simulated here. In these configurations, a boron atom (AB-B), nitrogen atom (AB-N) or both (AA) interact with one sublattice per atom, rather than interacting equally with both sublattices (as in the superlattice). Thus, a band gap opens. As the highly electronegative nitrogen interacts more strongly with the

graphene layer than boron does, the AA stacking opens the largest band gap (both boron and nitrogen interact with the graphene), the AB-N stacking opens a moderate band gap (only nitrogen interacts with the graphene), and the AB-B stacking opens the smallest band gap (only boron interacts with the graphene).

2. Electronic Dispersion

Unsurprisingly, the electronic band structures of the three h-C/BN bilayers strongly resemble the superposition of the single layer h-C and h-BN band structures, as shown in Fig. 7(a) and (b). Indeed, the in-plane, electron-ion interactions are much stronger than the cross-plane Van der Waals interactions. However, these small interactions do lift the symmetry between the graphene sublattices, such that a small band gap opens and the band edge gains dispersion at the K and K′ points, as predicted by the TB model.

The electronic band structure h-C:BN primarily resembles that of graphene. Note the limited dispersion in the π bands between the K and M points and the similarities between the σ bands near Γ, as displayed in Fig. 7(c). However, the π bands are depressed throughout the BZ and gain slight dispersion between Γ and K, among other substantial changes. Most importantly, a small band gap opens and the band edge gains dispersion, as predicted. Indeed, the TB model accurately predicts the qualitative features of the h-C:BN and h-C/BN π bands near the Fermi level.

3. Phonon density of states

The h-C/BN phonon density of states (D_p) very nearly equals the linear combination of the h-C and h-BN D_p, as shown in Fig. 8. While the asymmetry has important consequences for the electron band structure, the sp^2 bonds largely determine the phonon properties, and these bonds are nearly unaffected by the change in symmetry. Indeed, the only phonon features affected by the opening of the band gap are those which arise as a result of the strong *e-p* coupling in graphene and vanish as a result of this coupling weakening. For example, the Kohn anomaly of the TO phonon mode at K and K′ (A_1' mode) should weaken when the band gap opens, as the phonon no longer connects two points on the Fermi surface. However, accurately capturing this anomaly within DFT-LDA is difficult.[10] Therefore, the

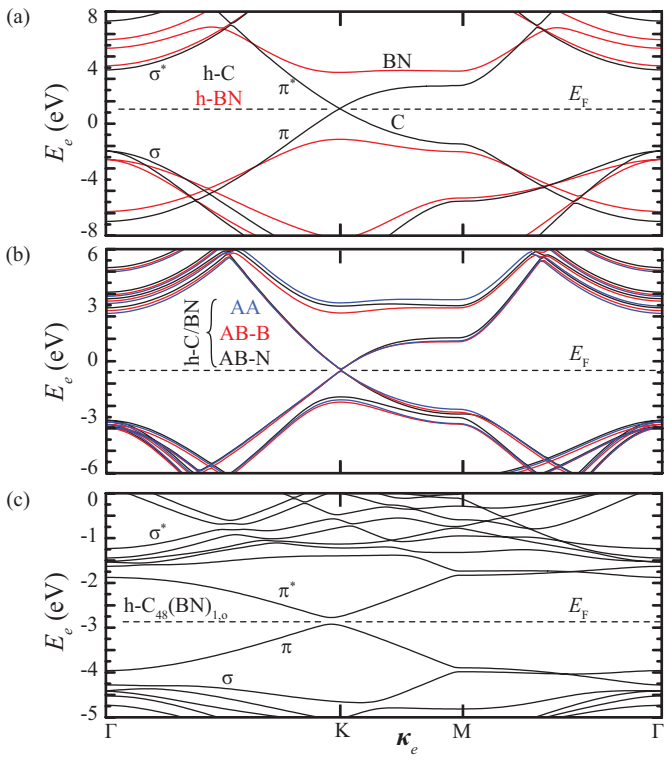

FIG. 7. The electronic structure of (a) h-C and h-BN, (b) h-C/BN, and (c) h-$C_{48}(BN)_{1,o}$. The band structure of h-C/BN strongly resembles the superposition of the h-C and h-BN band structures. The band structure of h-$C_{48}(BN)_{1,o}$, although complicated by the band-folding, resembles that of h-C. However, the π bands are less energetic and have some dispersion throughout the BZ. Note the narrow band gap formed in h-C:BN and h-C/BN and the large band gap of h-BN.

similarity between the phonon density of states in h-C, h-BN, and h-C/BN is both expected and produced.

Due to the computational requirements, calculating the dynamical matrices of h-C:BN for a grid of $\boldsymbol{k}_p$ points is unrealistic. With such a small collection of force constants, Fourier interpolation only captures some features of the density of states (DOS) well. These features strongly resemble the D_p in pure graphene, as expected for such a small concentration of BN. However, some differences are certain to exist, due to the differences in mass and harmonic force constants between B, C, and N atoms. The failure to capture these features would be particularly troubling if the *p*-*p* coupling were to be calculated for h-C:BN. However, such a calculation is already precluded by the large number of atoms, as discussed in Sec. V C 2. Moreover, the spectral functions of h-C:BN suggest that the disturbance is minimal when

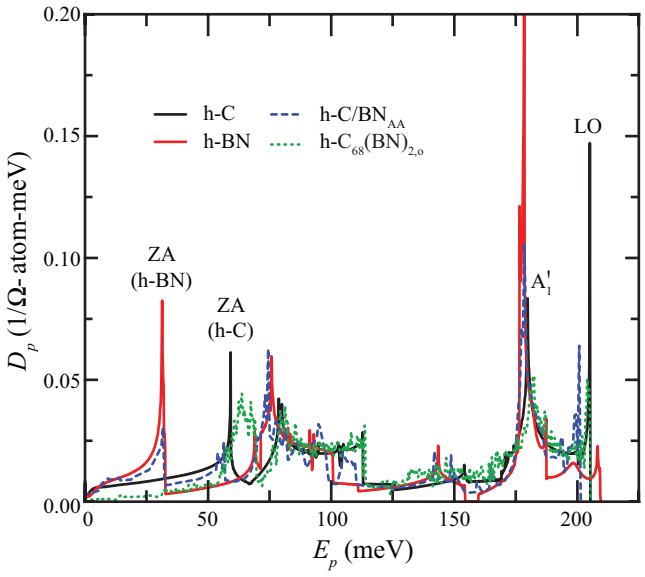

FIG. 8. The phonon density of states (D_p) for h-C:BN and h-C/BN. The density of states in h-C/BN is nearly the superposition of that in h-C and h-BN. While the density of states in h-C:BN strongly resembles that of h-C, the h-C:BN D_p calculation uses a single *ab initio* dynamical matrix (at $\boldsymbol{k}_p = \Gamma$). Therefore, the D_p is not as well resolved.

the BN concentration is below 6%, as discussed in Sec. V C 3.

C. Phonon interactions

The interaction of the E_{2g} phonon mode, i.e., the 198 meV Γ-point LO mode, with electrons, acoustic phonons, and defects is considered in this section, using the equations discussed in Sec. III.

1. Electron-phonon coupling

The interband electron-phonon scattering rate given in Eq. (6) requires the valence and conduction band structures ($E_{\boldsymbol{k}_e,i}$) and the interaction matrix elements [$M_{ep,\alpha,i,j}(\boldsymbol{k}_e, \boldsymbol{k}_p)$]. The matrix elements are evaluated within DFPT on the $\boldsymbol{k}_e$-mesh given in Sec. V A, while the band structures are collected from an additional, non-self-consistent electronic calculation on a dense $\boldsymbol{k}_e$-mesh (180×180 for h-C and h-C/BN and 18×18 for h-C:BN). Then, the band structure and matrix elements are linearly interpolated onto a fine 2000×2000 $\boldsymbol{k}_e$-mesh and

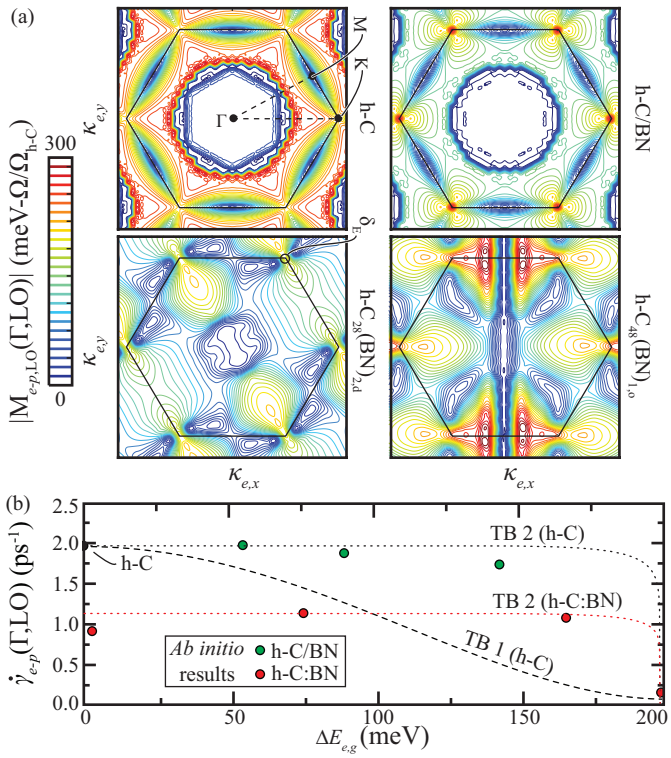

FIG. 9. *Ab initio* (a) Interband *e-p* coupling and (b) *e-p* scattering rate in h-C, h-BN, h-C/BN, and h-C:BN for the zone-center, LO phonon mode. The BZ and high symmetry points are shown, along with the ring for which energy is conserved ($\delta_{\rm E}$). Also shown are two TB models: TB 1, which uses a scaled overlap integral [Eq. (27)] as the *e-p* matrix element; and TB 2, which assumes the matrix element is independent of the band gap. The scattering rate is approximately halved when h-C is doped with BN. However, the *e-p* coupling remains strong at the K and K′ points, regardless of the asymmetry and band gap. Therefore, $\dot{\gamma}_{e-p}$ is nearly independent of $\Delta E_{e,g}$ until $\Delta E_{e,g} \simeq E_{p,\rm O}$, at which point the number of states available for interband transitions vanishes. The TB 2 model predicts this trend.

the integration [Eq. (6)] is carried out using a Lorentzian δ-function with 20 K of smearing, as in Phonovoltaic II.[2]

The *ab initio* interband electron-phonon coupling strength of the Γ-point LO phonon is shown in Fig. 9(a), where it is scaled by the relative area of the supercell ($\Omega/\Omega_{\rm h-C}$, where $\Omega_{\rm h-C}$ is the area of the graphene unit cell). The *e-p* coupling in graphene has a few notable features. First, the coupling vanishes near the Γ-point (between the σ and σ^* bands). In Phonovoltaic II[2], this result is used to suggest that the transformation from sp^2 to sp^3

hybridization destroys the *e-p* coupling in graphame (h-C:H). Second, the *e-p* coupling is relatively strong at the Dirac points. As the collection of energy conserving transitions form a small ring around these points (K and K′), this enables fast $\dot{\gamma}_{e-p}$. Both h-C:BN and h-C/BN exhibit these two features, as shown in Fig. 9(a).

This is unexpected: the TB model predicts that the conduction and valence band-edge wavefunctions are comprised of a different and orthogonal set of atomic orbitals, such that the *e-p* coupling should vanish at the K points, as discussed in Sec. IV. This is particularly unexpected in h-C/BN, where the h-BN substrate primarily effects the sublattice symmetry of the h-C layer, without substantially affecting the local properties. A partial explanation of this discrepancy comes from the assumption of orthogonality in the TB model: That is, the overlap integral is at least equal to the overlap of the nearest neighbor orbitals ($I^{\pm}_{\boldsymbol{k}_e,\boldsymbol{k}_e} \geq \langle p_{z,1}|p_{z,2}\rangle$). Therefore, if the orbitals centered on one atom overlap substantially with those centered on the nearest neighbor, the overlap integral remains substantial, even as $\Delta E_{e,g} \to E_{p,\mathrm{O}}$.

Two tight-binding models of the interband *e-p* scattering rate are derived in order to examine this behavior and determine the $\dot{\gamma}_{e-p}(\Delta E_{e,g})$ trend. Both models use the TB band structure [Eq. (23)] and the FGR integration presented in Eq. (6). However, they use different matrix elements. The first model (TB 1) uses the TB overlap integral [Eq. (27)] as the matrix element, while the second model (TB 2) assumes the matrix element is independent of the asymmetry. The scattering rate predicted by either model only depends on $\Delta E_{e,g}/E_{p,\mathrm{O}}$, and not on the individual parameters: $E_{p,\mathrm{O}}$, φ_h, ϵ_1, and ϵ_2. Therefore, these models are fit to the *ab initio* results by setting $E_{p,\mathrm{O}} = 198$ meV and then scaling $\dot{\gamma}_{e-p}$ to minimize the error between the predictions and the h-C, h-C:BN, or h-C/BN results.

As shown in Fig. 9(b), the TB 1 model predicts a steady decrease in $\dot{\gamma}_{e-p}$ with increasing $\Delta E_{e,g}$, while the TB 2 model predicts that $\dot{\gamma}_{e-p}$ is relatively independent of $\Delta E_{e,g}$ until $\Delta E_{e,g} \to E_{p,\mathrm{O}}$, at which point it vanishes. Indeed, the increasing dispersion at the valence and conduction band edges compensates almost exactly for the increasing band gap, such that the number of energy conserving transitions remains nearly constant as the band gap increases. When $\Delta E_{e,g} \to E_{p,\mathrm{O}}$, however, the number of energy conserving transitions vanishes quickly, such that $\dot{\gamma}_{e-p} \to 0$. The *ab initio* results agree extremely well with the TB 2 model. Indeed, the *e-p* coupling is nearly independent of the band gap in both h-C/BN and h-C:BN.

However, the *e-p* scattering rate in h-C:BN is half of that in graphene. Interestingly, this is not a function of the asymmetry: Note that the scattering rate in h-C/BN nearly equals that in graphene, regardless of the band gap (and thus the magnitude of the asymmetry). Moreover, note that the weakest *e-p* coupling occurs in h-$C_{28}(BN)_{2,d}$, which has the smallest band gap and least asymmetry. As this crystal has the highest BN concentration, it is likely that the effects of the BN pairs on the local electron behavior[41] weaken the *e-p* coupling. While the asymmetry – symmetry axis provides a useful tool with which to predict the band gap, dispersion, and trend in $\dot{\gamma}_{e-p}(\Delta E_{e,g})$, it is incapable of predicting the *e-p* coupling itself, particularly in a complex tuned-graphene crystal like h-C:BN.

2. Phonon-phonon coupling

The *ab initio* calculation of the *p-p* coupling remains impossible for h-C:BN, due to the computational demand involved in gathering the third-order energy derivatives. Thus, it is calculated only for h-C/BN and h-C. This enables an investigation of the effects the sublattice asymmetry has on the *p-p* interaction.

The third-order force constants are evaluated on a 9×9 $\boldsymbol{k}_p$ mesh within Quantum Espresso using the $2n+1$ formula.[42] These are then Fourier interpolated onto a $200\times200\times1$ mesh of $\boldsymbol{k}_p$ points. Then, the integration in Eq. (9) is carried out using a Lagrangian δ-function with 50 K smearing, as in Phonovoltaic II.[2]

The results for h-C and h-C/BN are presented in Fig. 10. The h-C results agree well with DFT-LDA calculations performed by Bonini *et al.*[11] Although the LA-TA mode is found to contribute less to the rate of down-conversion, the overall rate is nearly identical. Indeed, the electron-phonon and phonon-phonon scattering rates evaluated here for graphene combine to reproduce the experimental E_{2g} phonon lifetime[43], as in [11].

Moreover, the *p-p* coupling in h-C is nearly unaffected by the disruption of the sublattice symmetry caused by the adjacent h-BN layer. The primary difference is the slight suppression of the LA-TA pathway. For the same reasons that the phonon density of states remains essentially unchanged in the graphene layer, the phonon-phonon scattering rate also remains unchanged. That is, the sp^2 bonds primarily dictate the phonon behavior, and the electrons involved in these bonds are nearly unaffected by the h-BN substrate.

However, similar arguments are less convincing when applied to the h-C:BN crystals for

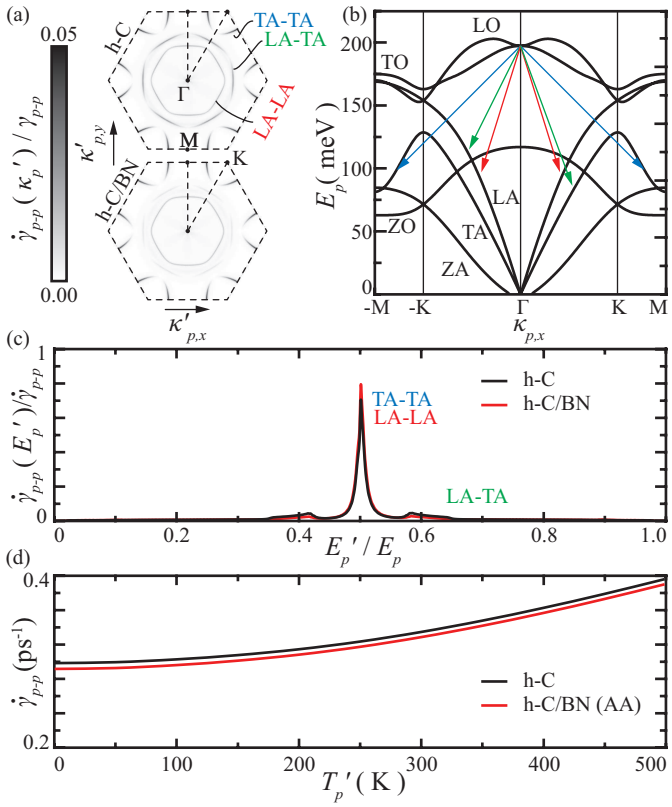

FIG. 10. (a) The *p*-*p* coupling in the first BZ, (b) down-conversion pathways, (c) down-converted phonon energy distribution, and (d) down-conversion rates in h-C and h-C/BN. (a), (b), and (c) combine to show the momentum and energy of the acoustic phonon modes produced during down-conversion of the LO phonon. These results show that the *p*-*p* coupling is nearly unaffected by the disruption of the sublattice symmetry, such that the down-conversion rate of h-C/BN approximately equals that in graphene.

which a *p*-*p* calculations remain impossible. While the phonon density of states in these crystals strongly resembles that in pure h-C, there are un-resolved and rough areas of the D_p which may hide the contributions of the BN pairs. Moreover, the literature lacks a close examination of the phonon lifetimes in h-C:BN. The closest study uses MD to calculate the phonon-phonon lifetime in h-C|BN heterostructures with 50% BN.[44] The lifetime of most optical phonon modes remains unaffected by the heterostructures. However, there is a dip in the lifetime of some optical phonon modes around 200 meV when the distance between h-C and h-BN interfaces grows. That is, these results show that even at 50% BN concentration, the phonon-phonon coupling is not necessarily enhanced by the addition of BN, but by the

period of the h-C|BN heterostructure. While definitive results remain elusive, the phonon-phonon scattering rate in pure graphene is used to characterize the phonovoltaic performance of an h-C:BN pV cell.

3. Phonon-defect coupling

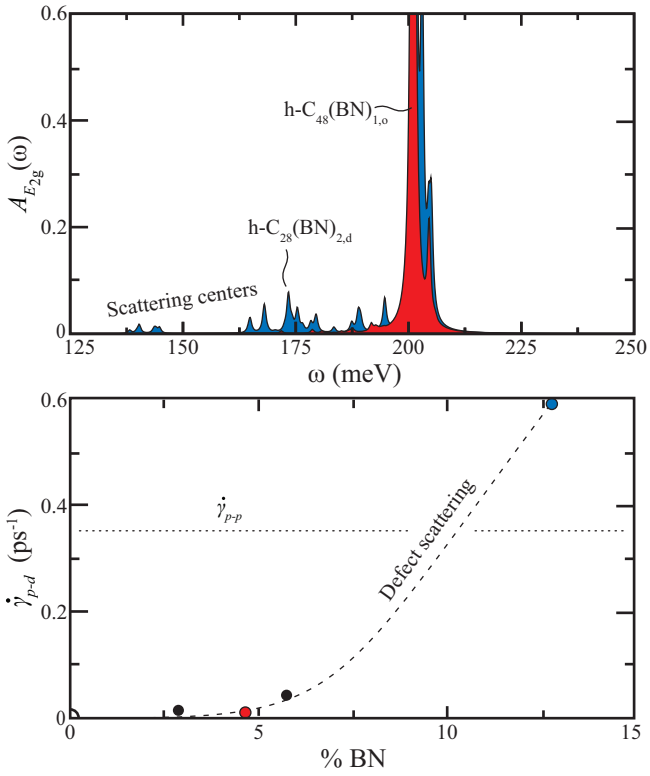

FIG. 11. (a) Spectral function and (b) defect scattering rate for h-C:BN. While the rate of scattering is negligible at a low BN concentration, it increases substantially with the BN concentration. However, only a small BN concentration is required to tune the band gap to the optical phonon energy.[24]

As the phonon spectral function only requires evaluation of the harmonic force constants, it remains feasible to calculate the phonon-defect scattering in h-C:BN. First, the DFT-LDA dynamical matrices are collected for pure graphene and for h-C:BN. Then, the ideal graphene dynamical matrix is diagonalized in order to gather the phonon eigenvectors, and a Lanczsos method is used to evaluate $G_{\boldsymbol{k}_p,\alpha}(\omega)$ [Eq. (13)].[35] Next, the spectral function is evaluated according to Eq. (12). Finally, a Lorentzian function is fit to $A_{\boldsymbol{k}_p,\alpha}(\omega)$, and the

scattering rate is given by the full-width at half-maximum of that Lorentzian.[34]

The results, presented in Fig. 11(a), show that only a few peaks exist in the spectral function near the optical phonon energy. Therefore, the optical phonon does not have many defect modes with which to scatter. Indeed, the predicted scattering rate is negligible at sufficiently low concentration. In contrast, the isotopic scattering rate predicted by Eq. (11) is comparable to the rate of down-conversion and would severely impact the phonovoltaic performance, even at a 5% BN concentration. However, as the decrease (increase) in mass for a boron (nitrogen) atom is compensated by weaker (stronger) force constants, the defect scattering rate of the E_{2g} mode remains negligible below 6% BN, which is sufficient to tune the band gap to the optical phonon energy. Indeed, experimental results suggest only 2% BN is required to open a 200 meV band gap.[24] Therefore, phonon-defect scattering is not important in a h-C:BN phonovoltaic.

Additionally, these results support the use of the h-C phonon-phonon down-conversion rates when evaluating a h-C:BN phonovoltaic. That is, if the spectral function has multiple, substantial peaks, it indicates that the perturbed lattice substantially affects the phonon dispersion and density of states. This, in turn, indicates that the anharmonic terms and resulting $\dot{\gamma}_{p-p}$ could be effected by the BN dopants. However, at low BN concentration, the spectral function exhibits very few off-center peaks. Therefore, it remains likely that the $\dot{\gamma}_{p-p}$ in h-C:BN nearly equals that in h-C.

VI. GRAPHENE:BN PHONOVOLTAICS

With the *ab initio* band gap ($0 < \Delta E_{e,g} < E_{p,\mathrm{O}}$), phonon energy (nearly constant at 198 meV), and scattering rates (assuming $\dot{\gamma}_{p-p}$ remains constant, as discussed in Sec. V C 2), the pV figure of merit and efficiency are evaluated according to Eqs. (1) - (3). Here, the diode equations described in Phonovoltaic I[1] are used to calculate the fill-factor, decreasing heat flux, and resulting efficiency. Figure 12 presents these *ab initio* results and the predicted phonovoltaic performance. In addition, the TB 2 *e-p* coupling model discussed in Sec. V C 1 is used to predict the performance of h-C:BN for $0 \leq \Delta E_{e,g} \leq E_{p,\mathrm{O}}$.

As shown, a h-$C_{68}(BN)_{2,o}$ pV cell can achieve a figure of merit around 0.6 and an efficiency around $0.4\eta_{\mathrm{C}}$. This is a substantial improvement on the previous study[2], which found that h-C:H pV cells had a negligible figure of merit and efficiency. More importantly, it is a

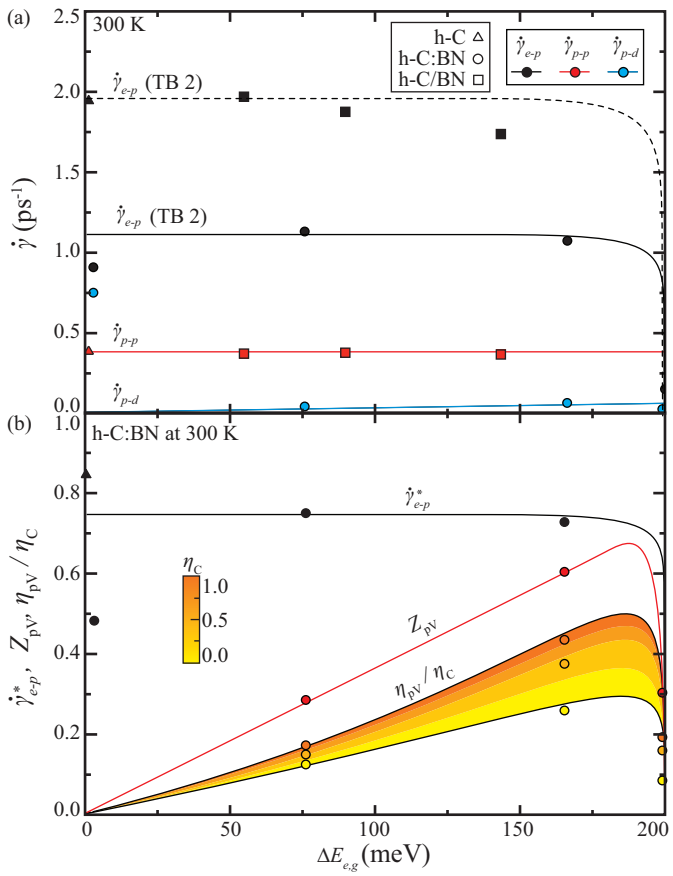

FIG. 12. (a) The optical phonon scattering rates of h-C, h-BN, h-C/BN, and h-C:BN and (b) resulting h-C:BN performance metrics. The TB 2 model (Sec. V C 1) is used to model the $\dot{\gamma}_{e-p}$ trends and interpolate performance between the *ab initio* h-C:BN results. While the incorporation of BN in h-C disrupts its strong *e-p* coupling, $\dot{\gamma}_{e-p}$ remains much faster than $\dot{\gamma}_{p-p}$ until $\Delta E_{e,g} \rightarrow E_{p,\mathrm{O}}$. Moreover, the defect scattering rate remains negligible in comparison to both $\dot{\gamma}_{e-p}$ and $\dot{\gamma}_{p-p}$. Thus, the $\dot{\gamma}^*_{e-p}$ in h-C:BN remains near 0.75 and Z_{pV} nearly reaches 0.7 at $\Delta E_{e,g} = 181$ meV. As the non-equilibrium between optical phonon population and cell increase ($\eta_{\mathrm{C}} \rightarrow 1$), the fill factor of the cell increases, and the efficiency ($\eta_p V$) approaches the figure of merit (Z_{pV}) times the Carnot limit (η_{C}), as shown using the color gradation (Sec. I A).

substantial improvement on a typical thermoelectric generator: if the thermoelectric figure of merit is $ZT = 1$ and $\eta_{\mathrm{C}} = 0.5$, then its efficiency is only $\eta_{\mathrm{TE}} \approx 0.2\eta_{\mathrm{C}}$, half of the pV efficiency. Moreover, the TB 2 *e-p* coupling model predicts that a properly tuned h-C:BN pV cell achieves $Z_{\mathrm{pV}} \approx 0.7$, as shown in Fig. 12. Note that h-C/BN does not make a a good pV material, as the ideally stacked bilayers simulated here do not represent the Moire

superlattice that h-C/BN forms (See Sec. II B).

Finally, note that asymmetry neither decreases the *e-p* coupling strength (as discussed in Sec. V C 1) nor increases the *p-p* coupling strength (as discussed in Sec. V C 2). However, the substitution of BN into graphene does decrease the *e-p* coupling strength. Therefore, other tuned graphene materials may exceed the h-C:BN figure of merit, particularly when asymmetry is the primary mechanism by which the band gap is tuned. For example, when a strong electric field is applied to bilayer graphene, it lifts the sublattice symmetry without significantly disturbing the lattice. Therefore, it may reach an even higher Z_{pV} than h-C:BN does.

VII. CONCLUSIONS

The promise of the pV cell is summarized and the difficulties in finding and designing a promising material are discussed. Tuned graphene remains the most promising material candidate, as graphene has an energetic optical phonon mode (200 meV) that exhibits strong *e-p* coupling and weak *p-p* coupling. Phonovoltaic II[2] showed that hydrogenating graphene (to produce graphame) can be used to tune the band gap of graphene to the optical phonon energy, but it also showed that doing so substantially weakens the *e-p* coupling.

Here, the *e-p* coupling of tuned graphene is investigated within the context of a tight-binding (TB) model in order to explore this result and discover if tuned graphene can succeed in a pV cell. The TB models shows that disrupting the sublattice symmetry in graphene in order to open a band gap also weakens the *e-p* coupling near the (former) Dirac points.

An *ab initio* investigation of substitutional and layered h-C:BN compounds is carried out in order to investigate this prediction, open and tune the band gap of graphene, and, most importantly, find and describe a material with a high Z_{pV}. All of these goals are accomplished. That is, the band gaps of a various h-C:BN compounds are evaluated within DFT-LDA and a variety of h-C:BN cells are found with a band gap smaller than $E_{p,\mathrm{O}}$. The *ab initio e-p* coupling calculations show that the TB overlap model (TB 1) is very conservative as $\Delta E_{e,g} \to E_{p,\mathrm{O}}$: The *e-p* coupling remained substantial near the band edge in the h-C:BN simulations. Moreover, the phonon density of states in h-C is only slightly affected by the incorporation of BN and the *p-p* coupling remains unchanged, at least in the layered h-C/BN structures. Thus, h-C:BN can reach a high Z_{pV} when the band gap is

appropriately tuned.

Indeed, h-$C_{68}(BN)_{2,o}$ achieves a phonovoltaic figure of merit greater than 0.6. From previous analytical models, this implies that a h-$C_{68}(BN)_{2,o}$ pV cell achieves at least 20% of the Carnot limit. Moreover, at a Carnot limit of 50% and cell temperature of 300 K (600 K optical phonon temperature), a h-$C_{68}(BN)_{2,o}$ pV cell can reach an efficiency around 20%, nearly doubling the efficiency of a thermoelectric generator ($ZT = 1$) under the same conditions. Furthermore, an updated TB *e-p* coupling model (TB 2) predicts that an appropriately tuned h-C:BN crystal can reach $Z_{\mathrm{pV}} \approx 0.7$.

Thus, the promise of tuned graphene is realized through the substitution of BN into graphene. Moreover, the TB model and *ab initio* results suggest that h-C:BN is not unique in this regard. Provided the sublattice symmetry of a tuned graphene material is manipulated to open a gap between 150 and 200 meV, that material should achieve similar or even higher Z_{pV} and η_{pV}.

With a suitable material candidate identified, the next theoretical challenges in pV research include the following: the identification and modeling of an appropriate phonovoltaic system, including the optical phonon source (e.g., a pV cell harvesting phonons produced from the Joule heating in an adjacent graphene cell), and the identification of alternate materials (e.g., a graphene bilayer under an electric field). The experimental challenges include the following: the production of a high-quality h-C:BN crystal with a tuned band gap, the verification of the predicted *e-p* and *p-p* coupling strengths, and, most importantly, the demonstration of the pV effect.

ACKNOWLEDGMENTS

This work was supported by the NSF program on Thermal Transport and Processes (Award No. CBET1332807) and employed computing resources of the DOE National Energy Research Scientific Computing Center (Office of Science, Contract No. DE-AC02-05CH11231).

---

* kaviany@umich.edu

[1] C. Melnick and M. Kaviany, Phys. Rev. B **93**, 094302 (2015).

[2] C. Melnick and M. Kaviany, Phys. Rev. B **93**, 125203 (2015).

[3] O. Madelung, *Semiconductors: Data Handbook*, Springer, 2004.

[4] S. Adachi, *Properties of Group-IV, III-V, and II-IV Semiconductors*, Wiley, 2005.

[5] W. Strehlow and E. Cook, J. Phys. Chem. Ref. Data **2**, 163 (1973).

[6] M. Sluiter and Y. Kawazoe, Phys. Rev. B **68**, 085410 (2003).

[7] Y. Jiao, Chem. Commun. **47**, 11843 (2011).

[8] H. Zhang, Y. Luo, X. Feng, L. Zhao, and M. Zhang, Phys. Chem. Chem. Phys. **17**, 20376 (2015).

[9] S. R. J. Maultzsch, C. Thomsen, H. Requardt, and P. Odejón, Phys. Rev. Lett. **92**, 075501 (2004).

[10] S. Piscanec, M. Lazzeri, F. Mauri, A. Ferrari, and J. Robertson, Phys. Rev. Lett. **93**, 185503 (2004).

[11] N. Bonini, Lazzeri, N. Marzari, and F. Mauri, Phys. Rev. Lett. **99**, 176802 (2007).

[12] V. Periera, A. C. Neto, and N. Peres, Phys. Rev. B **80**, 045401 (2009).

[13] F. Guinea, M. Katsnelson, and A. Geim, Nat. Phys. **6**, 30 (2009).

[14] F. M. D. Pellegrino, G. G. N. Angilella, and R. Pucci, Phys. Rev. B **81**, 035411 (2010).

[15] C. Park et al., Phys. Rev. Lett. **115**, 015502 (2015).

[16] M. O. Goerbig, Rev. Mod. Phys. **83**, 1193 (2011).

[17] H. Liu, Y. Liu, and D. Zhu, J. Mater. Chem. **21**, 3335 (2011).

[18] M. N. et al., Phys. Rev. Lett. **115**, 13680 (2015).

[19] V. Georgakilas et al., Chem. Rev. **112**, 6156 (2012).

[20] M. Mazzoni, R. Nunes, S. Azevedo, and H. Chacham, Phys. Rev. B **73**, 073108 (2006).

[21] P. Shinde and V. Kumar, Phys. Rev. B **84**, 125401 (2011).

[22] X. Fan, Z. Shen, A. Liu, and J.-L. Kuo, Nano. **4**, 2157 (2012).

[23] R. Nascimento, J. Martins, R. Batista, and H. Chacham, J. Phys. Chem. C **119**, 5055 (2015).

[24] C.-K. Chang et al., ACS Nano **7**, 1333 (2013).

[25] B. Hunt et al., Science **340**, 1427 (2013).

[26] P. Moon and M. Koshino, Phys. Rev. B **90**, 155406 (2014).

[27] J. Singh, *Physics of Semiconductors and their heterostructures*, McGraw-Hill, Inc., 1 edition, 1993.

[28] S. Baroni, S. de Gironcoli, A. D. Corso, and P. Giannozzi, Rev. Mod. Phys. **73**, 515 (2001).

[29] M. Kaviany, *Heat Transfer Physics*, Cambridge University Press, 2nd edition, 2014.

[30] D. Ecsedy and P. Klemens, Phys. Rev. B **15**, 5957 (1976).

[31] G. Srivistava, *The Physics of Phonons*, Adam Hilger, 1990.

[32] O. Hellman and I. Abrikosov, Phys. Rev. B **67**, 144304 (2003).

[33] P. Klemens, Proc. Phys Soc. A **68**, 1113 (1955).

[34] N. Vandecasteele, M. Lazzeri, and F. Mauri, Phys. Rev. Lett. **102**, 196801 (2009).

[35] N. Vast and S. Baroni, Phys. Rev. B **61**, 9387 (2000).

[36] P. Wallace, Phys. Rev. **71**, 622 (1947).

[37] R. Saito, G. Dresselhaus, and M. Dresselhaus, *Physical Properties of Carbon Nanotubes*, Imperial, London, 1998.

[38] S. Reich, J. Maultzsch, C. Thomsen, and P. Ordejón, Phys. Rev. B **66**, 035412 (2002).

[39] P. Giannozzi et al., J. of Phys.: Cond. Matter **21**, 395502 (2009).

[40] N. Troullier and J. L. Martins, Phys. Rev. B **43**, 1993 (1991).

[41] For example, the local electron density of states departs notably from the TB picture, especially around the BN atoms.[23].

[42] X. Gonze and J.-P. Vigneron, Phys. Rev. B **39**, 13120 (1989).

[43] J. Yan, Y. Zhang, P. Kim, and A. Pinczuk, Phys. Rev. Lett. **98**, 166802 (2007).

[44] C. da Silva, F. Saiz, D. A. Romero, and C. Amon, Phys. Rev. B **93**, 125427 (2016).